



Cite this: *Lab Chip*, 2018, 18, 979

Colloidal lithography-based fabrication of highly-ordered nanofluidic channels with an ultra-high surface-to-volume ratio†

Shuli Wang,^a Yongshun Liu,^b Peng Ge,^a Qiqi Kan,^a Nianzuo Yu,^a Jing Wang,^c Jingjie Nan,^a Shunsheng Ye,^a Junhu Zhang, *^a Weiqing Xu^c and Bai Yang ^a

This article shows a new strategy for the fabrication of nanofluidics based on nanoscale gaps in nanopillar arrays. Silicon nanopillar arrays are prepared in a designed position by combining conventional photolithography with colloidal lithography. The nanogaps between the pillars are used as nanochannels for the connection of two polydimethylsiloxane-based microchannels in microfluidics. The gap between neighbouring nanopillars can be accurately controlled by changing the size of initial colloidal spheres and by an etching process, which further determines the dimensions of the nanochannels. At a low ionic strength, the surface charge-governed ion transportation shows that the nanochannels possess the same electrokinetic properties as typical nanofluidics. Benefiting from the advantage of photolithography, large-area nanochannel arrays can be prepared in a parallel manner. Due to the perm-selectivity of the nanochannels, the nanofluidic chips can be used to preconcentrate low concentration samples. The large-area ordered nanostructures preserve their high-throughput property and large surface-to-volume ratio, which shows their great potential in the development of nanofluidics and their applications, such as in the separation of small molecules, energy conversion, etc.

Received 11th December 2017,
Accepted 16th February 2018

DOI: 10.1039/c7lc01326d

rsc.li/loc

1. Introduction

Over the past two decades, nanofluidic technologies, a natural extension of microfluidics and nanotechnology, have attracted significant attention and captured the imagination of many researchers.^{1–6} In general, nanofluidic devices are nanochannels with sizes less than 100 nm in one dimension. In such nanochannels, the channel size scales down to the interaction range of various surface/interface forces, and the surface properties of the channels play important roles in the fluid and molecular transportation in the nanochannels, which gives rise to unique and rich physical and chemical phenomena, such as electrical double layer overlap effects, ion concentration polarization, and nanofluidic rectification effects.^{1,7–11} These properties have been utilized in the development of a variety of sensitive biochemical sensors,^{12,13}

novel ionic devices,^{14,15} efficient energy harvesters,^{16–18} and other devices.¹⁹

The development of lab-on-a-chip (LOC) devices heavily depends on the micro and nanofabrication technologies. To date, many techniques have been developed to fabricate nanofluidic devices with precisely tailored feature sizes and functions.^{3,20–22} Conventional nanochannel fabrication methods include photolithography, electron beam lithography, focused ion beam milling, and nanoimprint lithography.^{5,20,21,23} The advantages of these nanofabrication methods are high resolution and reproducibility, however, the high complexity and fabrication costs limit their rapid prototyping and utilization in resource-limited settings. Recently, unconventional nanofabrication technologies have been developed to compensate for this or substitute conventional technologies.⁵ For example, techniques based on sacrificial films or nanowires^{24,25} and the mechanical deformation behaviors of elastomeric materials, including wrinkling,²⁶ cracking,²⁷ and structure collapsing,²⁸ have been employed to fabricate nanofluidic channels. These techniques facilitate the use of disposable nanofluidic devices in many applications with reduced cost and time, but they also possess some weaknesses in repeatability and reproducibility with high resolution.

Nanofluidic devices typically require microchannels to guide samples to the corresponding nanochannels, thus, the

^a State Key Laboratory of Supramolecular Structure and Materials, College of Chemistry, Jilin University, Changchun, 130012, P. R. China.
E-mail: zjh@jlu.edu.cn

^b State Key Laboratory of Applied Optics, Changchun Institute of Optics, Fine Mechanics and Physics (CIOMP), Chinese Academy of Sciences, 130033, P. R. China

^c State Key Laboratory of Supramolecular Structure and Materials, Institute of Theoretical Chemistry, Jilin University, Changchun, 130012, P. R. China

† Electronic supplementary information (ESI) available: Fig. S1–S9 and Videos S1 and S2. See DOI: 10.1039/c7lc01326d

demand for hybrid-scale LOC devices has been continuously increasing, focusing substantial attention on high-throughput, efficient, and reliable micro-nanofabrication methods.²⁰ Although various nanofabrication methods have been established to fabricate nanofluidic devices, simple and cost-effective PDMS-based soft lithography in microfluidics is still highly desirable in the development of nanofluidic devices.³ In addition, another barrier to the advancement of nanofluidic devices is the throughput (functional cross-sectional area) of the nanofluidic devices. In many applications, such as ionic devices and energy conversion devices, a high throughput is necessary, which obviously cannot be met easily by conventional nanochannels.²⁹ Nanofluidic crystals, which utilize the nanoscale space of close-packed nanoparticle arrays as nanofluidic channels, have provided an ultra-high throughput compared to conventional nanochannels.³ But such 3-dimensional nanochannels also exhibit some weaknesses in size controllability and integration with planar micro and nanochannels.

In this paper, we report a new strategy for the fabrication of nanochannels based on nanoscale gaps in nanopillar arrays. Colloidal lithography, which combines self-assembly of colloidal crystals with various colloidal crystal-assisted nanofabrication methods, has been recognized as a facile, low-cost, repeatable, and efficient nanofabrication technique for the fabrication of ordered nanostructure arrays, including nanopillars, nanoparticles, nanopores, nanowires, *etc.*^{30,31} Here, ordered nanopillar arrays were prepared in a designed position by combining conventional photolithography with colloidal lithography. After building a PDMS microchannel slab on a structured Si surface, the nanogaps between two adjacent nanopillars were used as nanoscale junctions for the connection of two microchannels. The gap between two adjacent pillars could be accurately controlled by changing the size of initial colloidal particles and the etching conditions, which further determines the dimensions of the nanogaps. Benefiting from the advantage of photolithography, large-area nanochannel arrays could be prepared in a parallel manner. Due to the perm-selectivity of the nanochannels, the micro-nano chip could be used to preconcentrate low concentration samples. In addition, the massively-ordered nanostructures provide a large surface-to-volume ratio, which is hard to achieve by conventional nanochannel fabrication methods.

2. Experimental

2.1 Materials

Silicon and glass substrates were cleaned by immersion in piranha solution (7:3 concentrated H₂SO₄/30%H₂O₂) for 5 h at 70 °C to create a hydrophilic surface and rinsed repeatedly with Milli-Q water (18.2 MΩ cm⁻¹) and ethanol. The substrates were dried with nitrogen gas before use. The photoresist (BP212-37s positive photoresist) was purchased from Kempur Microelectronics, Inc. Polystyrene (PS) microspheres (1000 nm and 480 nm in diameter) were purchased from Janus New Materials Co. Ltd. SG-2506 borosilicate glass (with a

145 nm thick chrome film and a 570 nm thick positive S-1805 type photoresist, Changsha Shaoguang Chrome Blank Co. Ltd.) was applied as the initial wafer for the fabrication of the microchannel mold. The Sylgard 184 elastomer base and curing agent for polydimethylsiloxane were purchased from Dow Corning (Midland, MI). Ethanol, toluene and acetone were used as received.

2.2 Fabrication of Si nanostructures through colloidal lithography

Nanopillar structures were prepared in a designed position by combining photolithography with colloidal lithography. First, a photoresist film 2 μm in thickness was spin-coated onto Si substrates. After ultraviolet exposure with a photo-mask and developing, an exposed area with dimensions of 200 × 800 μm² appeared on the substrate with the photoresist film. After oxygen plasma treatment for 5 min (Harrick Plasma), a monolayer of close-packed PS spheres was deposited onto the substrate *via* an interfacial self-assembly process.³² Then, the PS monolayer was etched into a non-close-packed state using oxygen reactive ion etching (RIE), performed with a Plasmalab Oxford 80 Plus system (Oxford Instruments Co., UK). The RIE procedure was operated at a pressure of 10 mTorr, a flow rate of 50 sccm, and a radio frequency (RF) power of 100 W. Reactive ion etching of Si was performed with a gas mixture of CHF₃ at 30 sccm and SF₆ at 4 sccm using the as-prepared non-close-packed PS monolayer as the mask. The total gas pressure was 5 mTorr; the RF power and the inductively coupled plasma (ICP) power were 50 and 100 W, respectively. The etching times of PS spheres and Si were 7 and 1 min, respectively. After etching, the residual PS and photoresist were removed by sonication in ethanol, toluene and acetone for 5 min. During the etching process of Si, the PS sphere masks were also consumed and became smaller, which resulted in circular truncated cone-structured nanopillars after the etching process. The size of the nanopillars was tailored by changing the etching time of PS and Si.

2.3 Fabrication of PDMS-Si micro-nanochannel devices

Micro-nanochannel hybrid devices were prepared using the gaps between the ordered nanostructures as nanofluidic channels. A glass mold was fabricated by wet etching and PDMS microchannels were prepared by standard soft lithography.^{33,34} A PDMS slab with two microchannels about 100 micrometers apart was prepared. Before bonding, four channel wells were punched on the PDMS microchannel slab, and adhesive tape was used for cleaning debris or dust on the microchannel surfaces. Then, the PDMS slab and Si wafer with nanostructures were both treated with oxygen plasma for 5 min and bonded together. Due to the apparent profile of nanostructures on the Si substrate, the alignment of the PDMS microchannels and nanochannels was realized with the naked eye. The capillary flow of a solution labeled with

fluorescein sodium salt in the micro-nanofluidic chip was recorded using a fluorescence microscope (Olympus BX51).

2.4 Fabrication of PDMS–glass and Si–glass micro-nanochannel devices

The fabrication of PDMS–glass micro-nanofluidic chips was similar to that of PDMS–Si chips, except the RIE conditions of glass surfaces. The etching of the glass surface was performed in a gas mixture of CHF_3 at 30 sccm and Ar at 15 sccm, and the RF power was 250 W. The etching durations of PS spheres and Si were 7 and 4 min, respectively. To prepare Si–glass micro-nanofluidic chips, we conducted another photolithography and inductively coupled plasma dry etching (Alcatel 601E ICP) for 2 min to construct microchannels, which were connected by nanogaps on the same Si substrate.³⁵ The etching of Si for constructing microchannels was performed with a gas mixture of C_4F_8 , SF_6 and O_2 . The radio-frequency power was 1800 W. After removing the residual photoresist, the micro-nanochannel-patterned Si substrate and borosilicate glass with inlet and outlet holes were cleaned by immersing in piranha solution for 20 min. The Si substrate and borosilicate glass were bonded by an anodic bonding method (SUSS SB6E Substrate Bonder); the bonding temperature was 400 °C, the applied voltage was 600 V, and the applied pressure was 1000 mbar.

2.5 Electrical measurement

A Keithley 2611B sourcemeter was used to record the ionic current between two electrodes in the PDMS–glass micro-nano hybrid chips filled with electrolyte solutions of different ionic concentrations. The nanopillared area on the glass substrate was 1 mm in width and the two microchannels are about 110 μm apart. When a bias was applied on silver electrodes in two reservoirs, the ionic current only passed through the nanogaps between the nanopillars. I – V curves across the nanochannels were recorded with the bias linearly varied from -2 to 2 V and were used to calculate the ionic conductance. Potassium chloride (KCl) was dissolved in deionized water to prepare electrolyte solutions of different ion concentrations.

2.6 Electrokinetic preconcentration

Glass-PDMS chips were used to conduct the ion concentration polarization experiment. 1 mM KCl solution was added to both the left and right microchannels, and an external DC voltage of 60 V was applied across the nanochannels. In addition, 1 $\mu\text{g mL}^{-1}$ of a fluorescein sodium salt solution was used to observe the flow field and ion behaviors. The concentration behavior was recorded with a fluorescence microscope (Olympus BX51).

3. Results and discussion

3.1 Fabrication of Si nanopillars and nanochannels

Nanopillar arrays on the Si surface were prepared by combining conventional photolithography with colloidal lithography (Fig. 1). First, the selected area for nanostructure construc-

tion was exposed by photolithography on a Si wafer. Then, a monolayer of close-packed PS was deposited onto the substrate, and the RIE process of PS and Si was performed. After removing the residual PS spheres and the photoresist, nanopillar arrays were prepared in the selected area on the Si substrate. The scanning electron microscopy (SEM) image in Fig. 2a shows that the original PS sphere was about 1000 nm in diameter. As shown in Fig. 2b, the ordered nanostructures were arranged on a large scale, and the high magnification SEM images in Fig. 2c and d show that the nanopillars are 880 and 740 nm in bottom (D1) and top (D2) diameters, respectively, 90 nm in height (H), and the bottom (S1) and top (S2) gaps between the adjacent two pillars are 130 and 260 nm, respectively. The morphology of the nanopillars is also confirmed by atomic force microscopy (AFM)(Fig. S1†).

Micro-nanochannel hybrid devices were prepared using the gaps between the ordered nanostructures as nanofluidic channels. After oxygen plasma treatment, the nanostructured substrate was immediately bonded to a PDMS microchannel slab. Compared to conventional single nanochannels, the prepared nanochannels are massive, interconnected nanogap networks. We characterized the bonding between the PDMS surface and the structured Si substrate. As shown in the SEM and AFM images in Fig. 3, after peeling off the PDMS microchannel slab from the silicon substrate, a thin layer of PDMS appeared on the top surfaces of the nanostructures that were covered by the flat PDMS surface, while the pillars under the microchannel section preserved their original smooth state. From the height profile of the AFM images, we could speculate that the PDMS surface did not collapse into the nanogaps between the nanostructures, indicating that the massively-ordered nanostructures provided sufficient

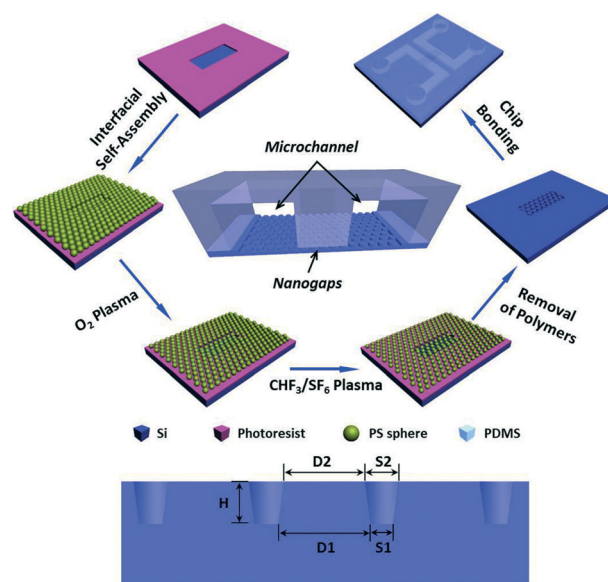


Fig. 1 Schematic illustration of the fabrication of nanochannels by combining conventional photolithography with colloidal lithography. The lower panel shows the geometric parameters of the Si nanostructures.

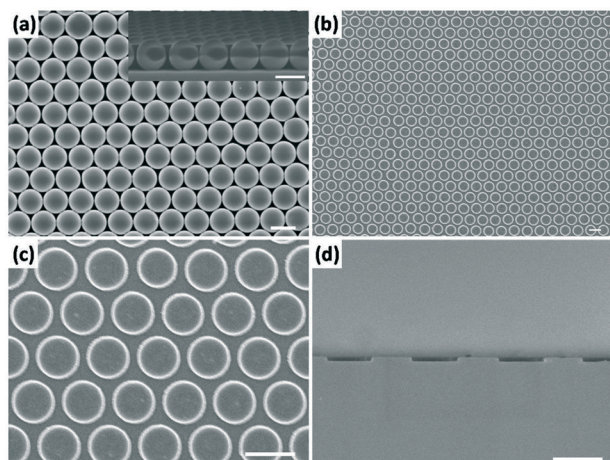


Fig. 2 (a) SEM images of close-packed PS colloidal sphere masks with a diameter of 1000 nm; the inset is the corresponding cross-sectional SEM image. (b) Low magnification SEM image of the obtained nanostructures. (c and d) High magnification planar and cross-sectional SEM images of the Si nanopillars. The scale bars are 1 μm .

mechanical strength for the upper low modulus PDMS slab and prevented the structure collapsing into the nanogaps. In addition, we did not observe a large unbonded area between the PDMS and Si nanopillars and the bonding was uniform in a large area (Fig. S2[†]), which confirm that the fluid could only transport through the nanogaps between the nanopillars. It is obvious that the throughput of this kind of

2-dimensional unconventional nanochannel is larger than that of the triangular-shaped nanochannel based on structure collapse (the general numerical calculation is shown in Fig. S3[†]), but it is still lower compared to the throughput of 3-dimensional nanofluidic crystals because they could be built on a scale of dozens to hundreds of micrometers. In addition, high-density nanopillar structures provide ultra-high surface areas compared to conventional nanoslit channels, which indicates that these nanochannels have great potential for the separation of proteins or nanoparticles on-chip.^{36,37}

Besides PDMS–Si chips, our fabrication method is also suitable for preparing PDMS–glass and Si–glass micro–nanofluidic chips. The fabrication of PDMS–glass micro–nanofluidic chips was similar to that of PDMS–Si chips, except for the reactive ion etching conditions for the glass surfaces. To prepare Si–glass micro–nanofluidic chips, we conducted another photolithography and inductively coupled plasma dry etching to construct microchannels, which were connected by nanostructures on the same Si substrate. After removing the residual photoresist and immersion in piranha solution, the micro–nanochannel-patterned Si substrate and borosilicate glass were bonded together by an anodic bonding method (Si–glass chips are shown in Fig. S4[†]).

3.2 Capillary filling in the nanochannels

The capillary flow of fluid in the micro–nanofluidic hybrid chip was recorded using a fluorescence microscope. As

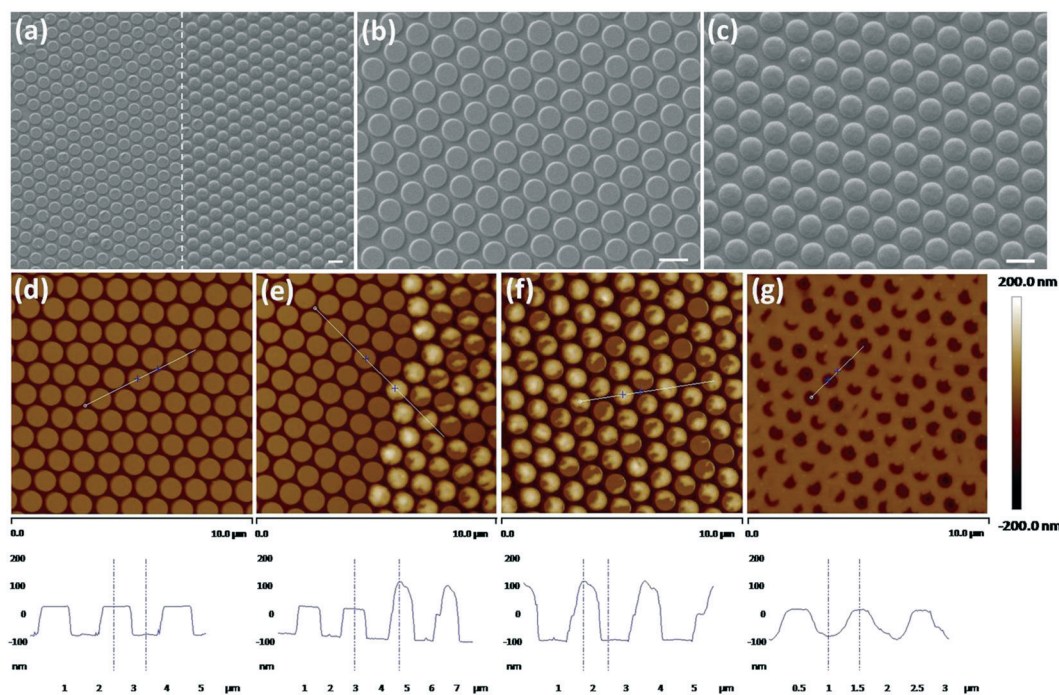


Fig. 3 (a)–(c) SEM and (d)–(f) AFM images of the Si pillars after peeling off the Si-pillared surface from the PDMS microchannel region and the flat PDMS surface. The left half part of images (a) and (e) and images (b) and (d) shows the Si pillars in the microchannel region; the right half part of images (a) and (e) and images (c) and (f) shows the Si pillars under the flat PDMS surface; the convex parts on the Si pillars indicate PDMS peeled off from the flat PDMS surface. (g) The PDMS holes were constructed after peeling off from the Si pillar region. The scale bars in (a)–(c) are 1 μm . The scale bars in AFM images (d)–(g) are 10 μm .

shown in Fig. 4a, two microchannels with a distance of about 100 μm are connected by nanochannels (the depth of the microchannels is about 25 μm). The nanostructures under the microfluidic channels exhibit a light brown color, while the pillars under the flat PDMS surface show a dark brown color. Since both the pillars and the PDMS surface were treated with oxygen plasma, the whole surfaces of the nanochannels were hydrophilic and water could transport in the nanochannels by capillary force. When one drop of an aqueous solution (about 10 μL in volume) was dropped into the inlet reservoir on the left side, it was transported into the channel due to the existence of capillary force. Water vapor formed near the nanojunctions, which led to the apparent color change of the nanostructures on the left side (Fig. 4b). The brown color of the pillars, either under the microchannel or the flat slab, became deeper (Fig. 4b–e), indicating the existence of fluid in the nanogaps between the pillars. Afterwards, water vapor formed in the microchannel on the right side, followed by the appearance of a deepened brown color of the nanostructures (Fig. 4f–h). When the fluid was transported to the right microchannel, another drop of the solution was dropped into the inlet reservoir on the right side, and it flowed through the microchannel (Fig. 4i–l); hence, the two microchannels were connected by the nanoscale gaps. The detailed capillary filling process is shown in Video S1.† The vapor of the solution may play an important role in the whole filling process, and the liquid in the nanogaps may

result from the condensation of the vapor.^{38,39} Fluorescence images were also taken to prove the existence of fluid in the nanochannels (Fig. S5†).

The properties of the surfaces become more and more dominant when the dimensions decrease to the microscale and nanoscale.^{3,40,41} For the nanochannels, the wetting property of the channel surfaces significantly influences the wetting and transportation of fluid in the channel. The original PDMS microchannel surface is hydrophobic when it is not treated with oxygen plasma. When the untreated hydrophobic PDMS microchannel was compressed onto the hydrophilic Si structures to construct a micro–nanofluidic chip, we could not observe an apparent color change in the pillars that connect two microchannels after fluid filling (Fig. S6†), because the fluid did not flow through the nanogaps due to the large Laplace pressure resulting from the top hydrophobic PDMS surface of the nanochannel. Therefore, hydrophilic treatment is essential for our PDMS–Si micro–nano chips, because plasma treatment not only facilitates the fluid transportation but also improves the bonding property of the chips.

3.3 Large-area nanochannel fabrication

Colloidal lithography provides a facile, low-cost, and efficient nanofabrication technique for ordered nanostructures on a large scale,³⁰ hence, it has potential for the construction of large-area nanochannels. Fig. 5a shows the SEM images of the nanopillar structures of the large-area nanochannels. After bonding the PDMS microchannel slab, capillary filling of the solution in the large-area nanochannels was recorded. The distance between the two microchannels connected by the nanostructures was 6.18 mm, and the bonding between the large-area nanostructures and the PDMS surface was uniform (Fig. S7†). When a drop of the solution was dropped into the inlet reservoir, it was transported into the microchannel and arrived at the nanopillars. In the nanochannels within such a large area, the aqueous solution was transported between the nanopillars and spread towards the other end. The fluid between the nanopillars changed the refractive index of the surrounding of 2-dimensional colloidal crystals, which led to an obvious change in structural color from dark blue to light green (Fig. 5a).⁴² The detailed flow process is shown in Fig. S8 and Video S2.† The front edge of the fluid in the large scale nanochannel was tracked, and the plot of distance (d) versus time (t) (Fig. 5f) is similar to the characteristic parabolic trend of a diffusion-limited phenomenon. Capillary filling of fluid is induced by the negative Laplace pressure and was first modeled by Washburn for circular channels and adapted to planar nanochannels by Han *et al.*

$$u = \sqrt{\frac{h\gamma \cos\theta}{2\eta}} \sqrt{t}$$

where u is the filling speed of liquid in the nanochannel, h is the height of the planar nanochannel, γ and θ are the surface tension of the liquid and the dynamic contact angle, respectively, and η is the viscosity of the liquid.^{43,44} The fluid filling

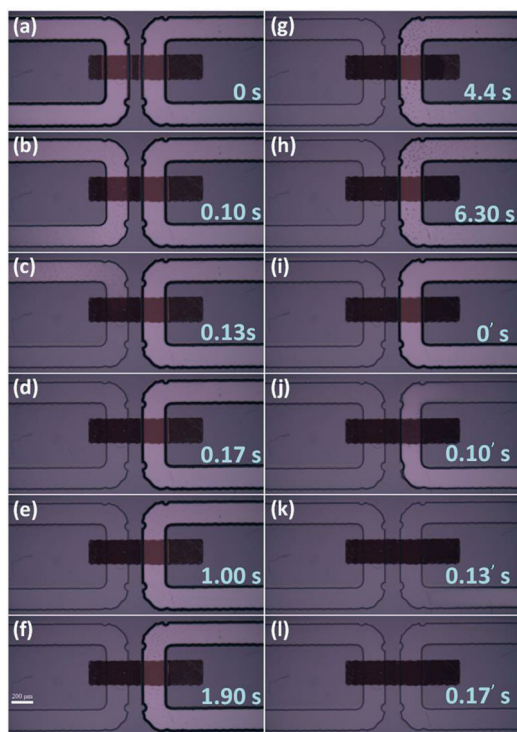


Fig. 4 Capillary flow of the aqueous solution in the micro–nanofluidic channel. Fluid transportation in the left microchannel, the nanogaps between the nanostructures (a–h) and the right microchannel (i–l). The scale bar is 200 μm .

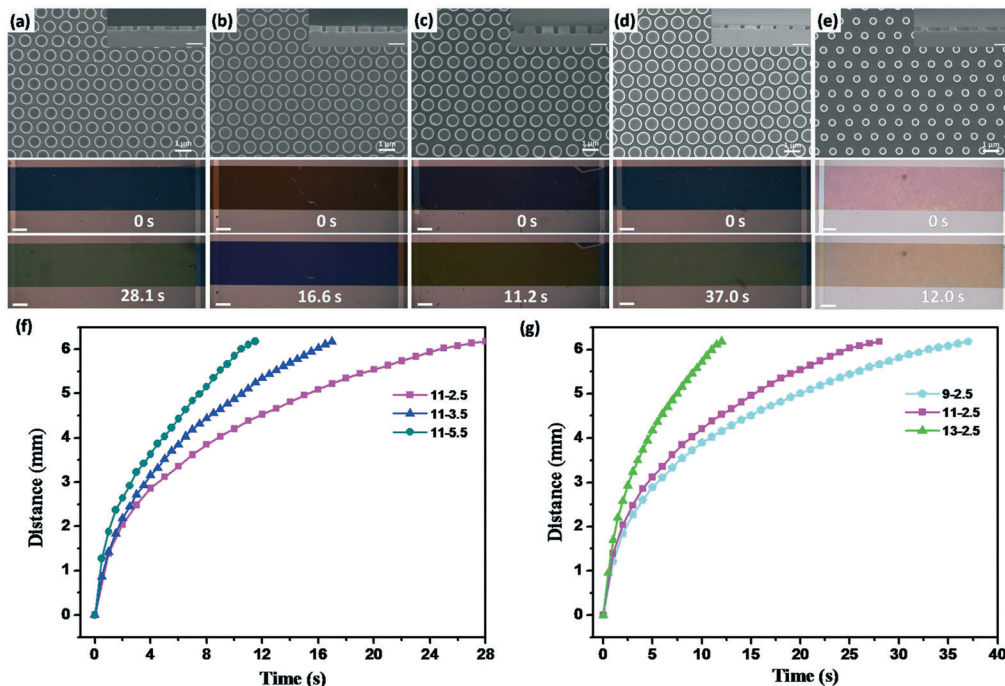


Fig. 5 SEM images of nanopillars with different dimensions for large-area nanochannel fabrication and microscopy images of the nanochannels before and after capillary filling. The etching times of PS-Si for the nanopillars in images (a)–(e) are 11–2.5 min, 11–3.5 min, 11–5.5 min, 9–2.5 min, and 13–2.5 min, respectively. The scale bars of the SEM images are 1 μm . The scale bars of the microscopy images are 500 μm . Diagram of the fluid front displacement *versus* time in nanochannels with (f) similar widths but different heights and (g) different widths but similar heights.

in the mesoporous pillared planar nanochannels was 4 to 6 times lower than that in pillar-free planar nanochannels.⁴⁵ In our system, the presence of the nanostructures significantly increases the quantity of interfaces and the apparent viscosity of the solution. The fraction of water molecules subjected to the hydration force at the solid interface is higher, which results in an increase in apparent viscosity.

The capillary filling in the nanochannels is affected by the dimensions of the nanogaps between the nanostructures, which could be accurately controlled through changing the etching duration of colloidal particles and silicon. The distance between the adjacent nanostructures could be controlled by changing the etching time of PS spheres, and the height of the nanochannels could be tailored by changing the etching duration of Si. Fig. 5a–e show the SEM images of nanogaps with different dimensions (taken from the center region of the patterned area). The nanogaps were uniform across the patterned area and the sizes of the nanogaps in the center region and along the edges were the same (Fig. S9†). Some defects and mismatch of the lattice affect the uniformity of the nanogaps, but these disordered nanogaps in very small areas are always surrounded by ordered nanogaps. Ordered nanostructures on a large scale are the integration of lots of small orderly arranged nanostructures. The etching conditions and the detailed dimension parameters of the prepared nanopillars are shown in Table 1. We changed the dimensions of the bottom gap from 190 to 560 nm by increasing the etching time of PS from 9 to 13 min; the height of the nanogaps increased from 240 to 480 nm when the etch-

ing duration of Si increased from 2.5 to 5.5 min. These nanopillars were used for large-area nanochannels and capillary filling of the aqueous solution in these nanochannels were studied. Due to the different sizes of the nanostructures, the fluid in the nanogaps showed different color changes, which facilitated the observation of fluid transportation in the nanochannels. As shown in the plot of distance *versus* time in Fig. 5f and g, the capillary filling speed of fluid was different in these nanochannels. The capillary filling speed is faster in the nanochannels with a large distance or high structures. For the nanochannels with different widths and heights, the apparent viscosity was high in the nanostructures with a smaller distance and height, which resulted in the decrease in filling speed.

Nanochannels with a large height to width ratio could also be prepared by this method. During the etching of Si, the PS sphere masks were also consumed and the diameter of the spheres was reduced. Thus, direct etching of Si was performed using original close-packed PS spheres as masks to prepare nanochannels with a large height to width ratio.

Table 1 Detailed parameters of the nanopillars prepared after etching of PS and Si for different times

$T_{\text{PS}}-T_{\text{Si}}$ [min]	D1 [nm]	D2 [nm]	S1 [nm]	S2 [nm]	H [nm]
11–2.5	730	660	280	340	240
11–3.5	780	680	220	320	330
11–5.5	760	680	240	320	480
9–2.5	810	720	190	280	230
13–2.5	440	350	560	650	250

When Si was etched for a short time, the obtained nanogaps were not connected (Fig. S10[†]); when the etching time increased to 8 min, the nanogaps were connected and nanochannels with a large height to width ratio ($670/70 = 9.57$) were obtained (Fig. 6a). In addition, the density of the pillars could also be tailored by using PS spheres with different diameters. Here, we used PS spheres 480 nm in diameter as etching masks and chose an etching time of 5 and 2 min for PS and Si, respectively. Fig. 6b shows the prepared high-density nanostructures. The simple controllability of the dimensions and density of the ordered nanopillars expand the potential of our method for different nanofluidic applications.

3.4 Electrokinetic properties

In nanochannels, the electrical double layer overlaps at a low ionic concentration and the surface properties of the channels play important roles in the molecular transportation in the nanochannels. To study the electrical characteristics of the nanochannels, the ionic current between two electrodes in the PDMS–glass micro–nano hybrid chips filled with electrolyte (KCl) solutions of different ionic concentrations was recorded using a sourcemeter. I – V curves across the nanochannels were recorded with the bias linearly varied from -2 to 2 V and were used to calculate the ionic conductance. Fig. 7a and b show the planar and cross-sectional SEM images of the glass nanostructures for the nanochannel preparation. As shown in Fig. 7c, the conductance increases with concentration almost linearly when the concentration is higher than 10^{-2} M (the dashed line depicts the conductance expected in the nanochannels from the conductivity of the

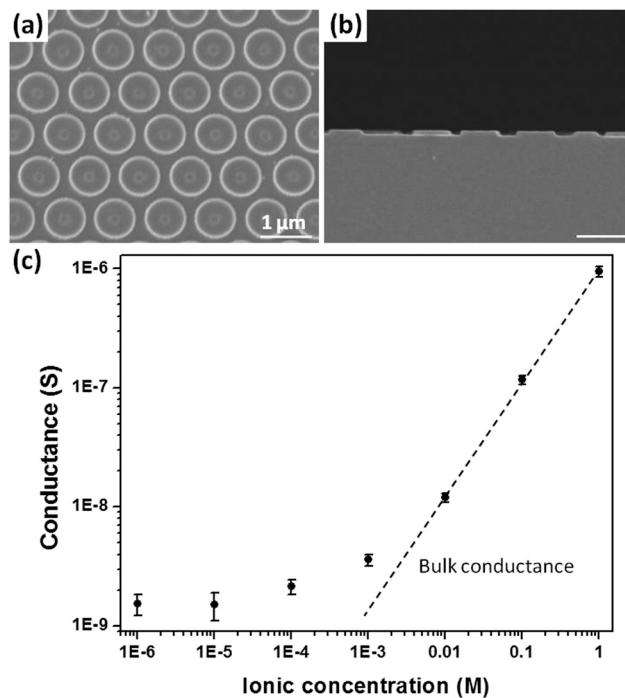


Fig. 7 (a) and (b) Planar and cross-sectional SEM images of the glass nanostructures (the etching time of PS and glass is 7 and 4 min, respectively). (c) Conductance of the aqueous solution-filled nanochannels as a function of the electrolyte concentration. The line depicts the conductance expected in the nanochannel from the conductivity of the bulk solution.

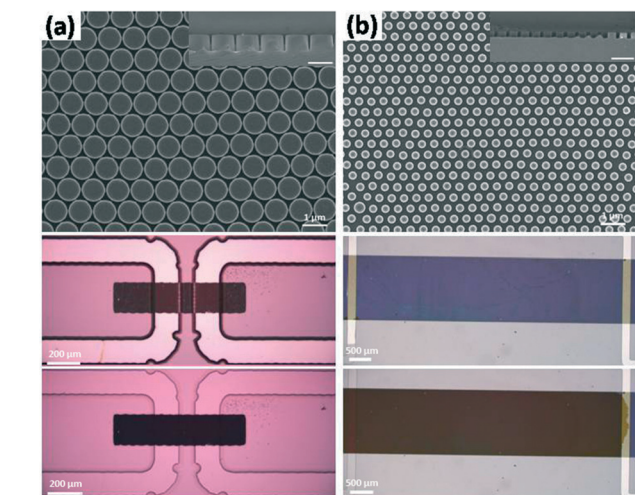


Fig. 6 (a) SEM image of the nanogaps with a large height-to-width ratio after direct etching of Si for 8 min; (b) SEM image of high-density nanogaps using 480 nm PS microspheres as etching masks; the etching time of PS and Si is 5 and 2 min, respectively. The insets show the corresponding cross-sectional SEM images. The scale bars are 1 μ m. Lower microscopy images show the corresponding micro-nanofluidic channels before and after fluid filling.

bulk solution). The conductivity of the nanochannel is strongly enhanced under the condition of low ionic strength compared with that of the bulk solutions with the same ionic strength because of the surface-charge-governed ion transport properties in the nanochannels.¹⁰ The averaged ionic conductance at a concentration of 10^{-6} M was comparable to that at a concentration of 10^{-5} M. This may have resulted from hydronium ions arising from the dissolution of carbon dioxide from the ambient atmosphere. The theoretical predictions and experimental results of Jensen *et al.* show that at a low ionic concentration (lower than 10^{-5} M), H^+ ions play an important role for the ionic conductivity of the nanochannels.⁴⁶ Therefore, the nanochannels based on the nanogaps between the nanostructures have the same electrokinetic properties as a single nanochannel.

Due to the nanoscale dimensions of the nanostructures, the electrical double layer overlaps in the nanochannels at a low ionic strength, which leads to the perm-selectivity of the nanochannels. Among the nanofluidic phenomena, ion concentration polarization is a direct and exact indication of the perm-selectivity of nanochannels.⁴⁷ This property could be utilized to concentrate a small amount of biomolecules in the microchannels. In our experiment, PDMS–glass chips were used to conduct the ion concentration polarization experiment (Fig. 8a), and the glass nanopillars shown in Fig. 7a and b were used. In our micro–nano hybrid system, glass and PDMS are both negatively charged at near-neutral

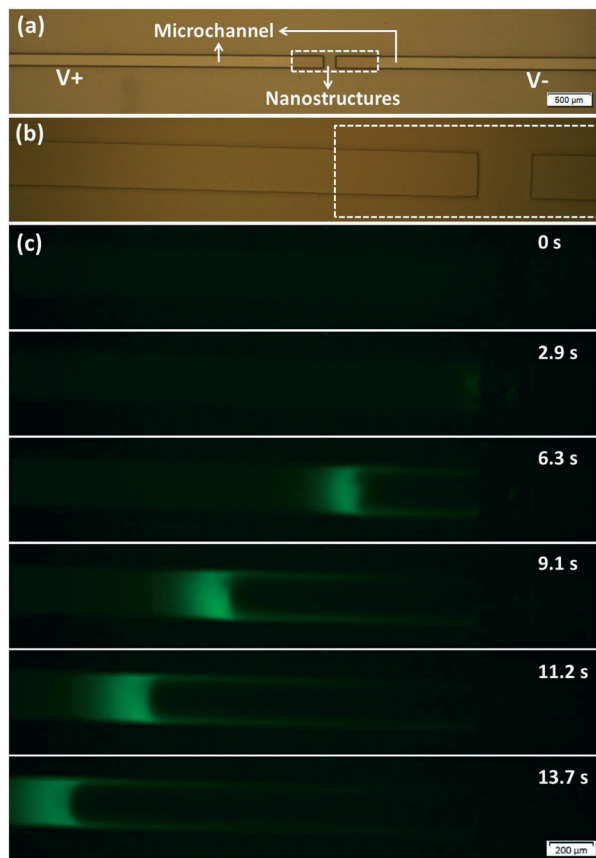


Fig. 8 (a) and (b) Microscopy image of the PDMS-glass chips for ion preconcentration. (c) Ion concentration behavior of sodium salt in the hybrid chip under an applied voltage of 60 V.

pH, thus, the nanochannel formed by the PDMS and glass nanostructures is cation-selective. A 1 mM KCl solution was added to both the left and right microchannels, and an external DC voltage of 60 V was applied across the nanostructures. To observe the flow field and ion behaviors, $1 \mu\text{g mL}^{-1}$ of a fluorescein sodium salt solution was added to the solution. The fluorescence images in Fig. 8c clearly show that an ion concentration plug was around the anodic end of the nanochannel. The preconcentration factor of the prepared nanofluidic device was measured based on the gray value of the microscopy images for different concentrations of fluorescein sodium salt solution using the same exposure time. There is a background gray value of pure water in the microchannel, thus, the real gray value resulting from the fluorescein sodium salt is calculated as follows:

$$G_{\text{real}} = G_{\text{apparent}} - G_{\text{background}}$$

The gray value after concentration for 11.2 s was 42.33 using our device, and the enrichment factor is 42.8 based on the curve of the gray value obtained at different concentrations (Fig. S11†). The preconcentration factor may be further increased by decreasing the size of the nanogaps or increasing the surface charge density of the nanochannel surfaces.

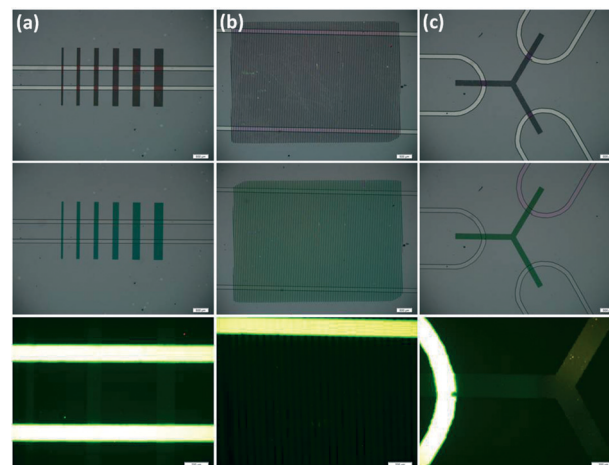


Fig. 9 Microscopy images of the nanochannels with different patterns before and after capillary filling of the aqueous solution: (a) stripe patterns with different widths; (b) large-area stripe arrays with the same width; (c) branched nanochannel patterns. The scale bars are 500 μm . The bottom images are the fluorescence images of the corresponding micro-nanofluidic channels; the scale bars are 200 μm .

Hence, the nanogaps in the nanopillar arrays could be used to concentrate low concentration samples.^{48,49}

3.5 Multiple micro-nanochannel designs

Since the structured region on the substrate was defined by photolithography, multiple nanochannel patterns and large-area nanochannels could be prepared in a parallel manner. For example, we fabricated nanochannels with different widths, where each nanochannel possesses different quantities of nanogaps, simply by using a photomask with stripes of different widths (Fig. 9a). We also prepared large-area stripe-patterned nanochannels, where each stripe could act as a nanochannel between the pillared stripes define the boundary of the nanochannel (Fig. 9b). Fig. 9c shows that a branched nanochannel that connects three microchannels was designed and constructed in a simple way, which may have promising applications in nutrition supply for cell or the transportation and analysis of small amounts of cell metabolites.⁵⁰ It is worth mentioning that the nanochannels on the same substrate were prepared in a parallel manner and the fabrication time for the aforementioned complex chips was comparable to single channel design, indicating that our method is labour- and time-saving for the fabrication of large-area and complicated micro-nanofluidic chips. In addition, the nanochannels based on nanogaps are compatible with conventional photolithography and microfluidic channels, which facilitates the integration of LOC devices with versatile functions.

Conclusions

This article presents a novel strategy for the fabrication of nanochannels based on the nanoscale gaps in nanopillar arrays. Si nanopillars were prepared in a designed position by

combining photolithography with colloidal lithography. The nanogaps between the pillars were used as nanojunctions for the connection of microchannels. The gaps between neighbouring nanopillars could be tailored by changing the size of initial colloidal spheres and by an etching process, which further determined the dimensions of the nanochannels. Due to the perm-selectivity of the nanochannels, the nanochannels could be used for the preconcentration of low concentration samples. Benefiting from the advantage of photolithography, large-area and complicated nanochannels could be prepared in a parallel manner. This nanochannel fabrication method is compatible with conventional photolithography and microfluidic channels, which facilitates the integration of LOC devices with versatile functions. Moreover, the nanochannels based on the nanogaps between the nanostructures preserve a high-throughput property and a large surface-to-volume ratio, which shows their great potential in the development of nanofluidics and their applications, such as separation of small molecules, energy conversion, *etc.*

Author contributions

S. Wang, P. Geng, Q. Kan, and N. Yu performed the nanofluidic chip design, fabrication, experiments, measurement, and analysis. Y. Liu patterned the silicon microchannel-nanostructure surfaces and bonded the patterned surfaces and glass cover plates. J. Wang and W. Xu measured the ionic conductance of the micro-nanofluidic chips. J. Nan and S. Ye performed the preconcentration of biomolecules. J. Zhang and B. Yang contributed to the idea. S. Wang and J. Zhang wrote the manuscript.

Conflicts of interest

There are no conflicts to declare.

Acknowledgements

This work was funded by the National Natural Science Foundation of China (Grant No. 21474037, 21774043, and 51505456), the Science and Technology Development Program of Jilin Province (20150520110JH), and the Jilin Province Development and Reform Commission (2015Y028). This project was also supported by the State Key Laboratory of Applied Optics.

References

- 1 W. Sparreboom, A. van den Berg and J. C. T. Eijkel, *Nat. Nanotechnol.*, 2009, **4**, 713–720.
- 2 L. Bocquet and E. Charlaix, *Chem. Soc. Rev.*, 2010, **39**, 1073–1095.
- 3 W. Ouyang, J. Han and W. Wang, *Lab Chip*, 2017, **17**, 3006–3025.
- 4 D. Mijatovic, J. C. T. Eijkel and A. van den Berg, *Lab Chip*, 2005, **5**, 492–500.
- 5 P. Abgrall and N. T. Nguyen, *Anal. Chem.*, 2008, **80**, 2326–2341.
- 6 M. Napoli, J. C. T. Eijkel and S. Pennathur, *Lab Chip*, 2010, **10**, 957–985.
- 7 H. Daiguji, *Chem. Soc. Rev.*, 2010, **39**, 901–911.
- 8 Z. Zhang, X.-Y. Kong, K. Xiao, G. Xie, Q. Liu, Y. Tian, H. Zhang, J. Ma, L. Wen and L. Jiang, *Adv. Mater.*, 2016, **28**, 144–150.
- 9 A. Piruska, M. Gong, J. V. Sweedler and P. W. Bohn, *Chem. Soc. Rev.*, 2010, **39**, 1060–1072.
- 10 R. Peng and D. Li, *Lab Chip*, 2016, **16**, 3767–3776.
- 11 D. Ha, J. Hong, H. Shin and T. Kim, *Lab Chip*, 2016, **16**, 4296–4312.
- 12 C. Duan, M. A. Alibakhshi, D.-K. Kim, C. M. Brown, C. S. Craik and A. Majumdar, *ACS Nano*, 2016, **10**, 7476–7484.
- 13 R. Karnik, K. Castellino, R. Fan, P. Yang and A. Majumdar, *Nano Lett.*, 2005, **5**, 1638–1642.
- 14 I. Vlassiuk, T. R. Kozel and Z. S. Siwy, *J. Am. Chem. Soc.*, 2009, **131**, 8211–8220.
- 15 I. Vlassiuk and Z. S. Siwy, *Nano Lett.*, 2007, **7**, 552–556.
- 16 F. H. J. van der Heyden, D. J. Bonthuis, D. Stein, C. Meyer and C. Dekker, *Nano Lett.*, 2006, **6**, 2232–2237.
- 17 W. Guo, L. Cao, J. Xia, F.-Q. Nie, W. Ma, J. Xue, Y. Song, D. Zhu, Y. Wang and L. Jiang, *Adv. Funct. Mater.*, 2010, **20**, 1339–1344.
- 18 Z. Zhang, X. Sui, P. Li, G. Xie, X.-Y. Kong, K. Xiao, L. Gao, L. Wen and L. Jiang, *J. Am. Chem. Soc.*, 2017, **139**, 8905–8914.
- 19 S. Wang and L. J. Lee, *Biomicrofluidics*, 2013, **7**, 011301.
- 20 C. Duan, W. Wang and Q. Xie, *Biomicrofluidics*, 2013, **7**, 026501.
- 21 D. Xia, J. Yan and S. Hou, *Small*, 2012, **8**, 2787–2801.
- 22 D. G. Haywood, A. Saha-Shah, L. A. Baker and S. C. Jacobson, *Anal. Chem.*, 2015, **87**, 172–187.
- 23 R. Chantiwas, S. Park, S. A. Soper, B. C. Kim, S. Takayama, V. Sunkara, H. Hwang and Y.-K. Cho, *Chem. Soc. Rev.*, 2011, **40**, 3677–3702.
- 24 K. S. Chu, S. Kim, H. Chung, J.-H. Oh, T.-Y. Seong, B. H. An, Y. K. Kim, J. H. Park, Y. R. Do and W. Kim, *Nanotechnology*, 2010, **6**, 425302.
- 25 F. Liang, A. Ju, Y. Qiao, J. Guo, H. Feng, J. Li, N. Lu, J. Tu and Z. Lu, *Lab Chip*, 2016, **16**, 984–991.
- 26 S. Chung, J. H. Lee, M.-W. Moon, J. Han and R. D. Kamm, *Adv. Mater.*, 2008, **20**, 3011–3016.
- 27 K. L. Mills, D. Huh, S. Takayama and M. D. Thouless, *Lab Chip*, 2010, **10**, 1627–1630.
- 28 S.-M. Park, Y. S. Huh, H. G. Craighead and D. Erickson, *Proc. Natl. Acad. Sci. U. S. A.*, 2009, **106**, 15549–15554.
- 29 Y.-A. Song, C. Batista, R. Sarpeshkar and J. Han, *J. Power Sources*, 2008, **183**, 674–677.
- 30 J. Zhang, Y. Li, X. Zhang and B. Yang, *Adv. Mater.*, 2010, **22**, 4249–4269.
- 31 J. Zhang and B. Yang, *Adv. Funct. Mater.*, 2010, **20**, 3411–3424.
- 32 J. Rybczynski, U. Ebels and M. Giersig, *Colloids Surf., A*, 2003, **219**, 1–6.

- 33 B.-Y. Xu, X.-N. Yan, J.-D. Zhang, J.-J. Xu and H.-Y. Chen, *Lab Chip*, 2012, **12**, 381–386.
- 34 S. Wang, T. Wang, P. Ge, P. Xue, S. Ye, H. Chen, Z. Li, J. Zhang and B. Yang, *Langmuir*, 2015, **31**, 4032–4039.
- 35 N. Yu, S. Wang, Y. Liu, P. Xue, P. Ge, J. Nan, S. Ye, W. Liu, J. Zhang and B. Yang, *Langmuir*, 2017, **33**, 494–502.
- 36 M. Azim, A. Malekpourkoupaei, W. Ye, A. B. Jemere and D. J. Harrison, *Electrophoresis*, 2017, **38**, 342–349.
- 37 N. Shaabani, A. B. Jemere and D. J. Harrison, *Electrophoresis*, 2016, **37**, 2602–2609.
- 38 D. Schneider, R. Valiullin and P. A. Monson, *Langmuir*, 2014, **30**, 1290–1294.
- 39 J. Zhong, S. H. Zandavi, H. Li, B. Bao, A. H. Persad, F. Mostowfi and D. Sinton, *ACS Nano*, 2017, **11**, 304–343.
- 40 J. W. van Honschoten, N. Brunets and N. R. Tas, *Chem. Soc. Rev.*, 2010, **39**, 1096–1114.
- 41 S. Wang, N. Yu, T. Wang, P. Ge, S. Ye, P. Xue, W. Liu, H. Shen, J. Zhang and B. Yang, *ACS Appl. Mater. Interfaces*, 2016, **8**, 13094–13103.
- 42 X. Zhang, S. Ye, X. Zhang, Z. Li, S. Wu, J. Zhang, T. Wang and B. Yang, *J. Mater. Chem. C*, 2013, **1**, 933–940.
- 43 E. W. Washburn, *Phys. Rev.*, 1921, **17**, 273.
- 44 A. Han, G. Mondin, N. G. Hegelbach, N. F. de Rooij and U. Staufer, *J. Colloid Interface Sci.*, 2006, **293**, 151–157.
- 45 M. Faustini, M. Vayer, B. Marmiroli, M. Hillmyer, H. Amenitsch, C. Sinturel and D. Grosso, *Chem. Mater.*, 2010, **22**, 5687–5694.
- 46 K. L. Jensen, J. T. Kristensen, A. M. Crumrine, M. B. Andersen, H. Bruus and S. Pennathur, *Phys. Rev. E: Stat., Nonlinear, Soft Matter Phys.*, 2011, **83**, 056307.
- 47 X. Yuan, L. Renaud, M.-C. Audry and P. Kleimann, *Anal. Chem.*, 2015, **87**, 8695–8701.
- 48 B. Kim, J. Heo, H. J. Kwon, S. J. Cho, J. Han, S. J. Kim and G. Lim, *ACS Nano*, 2013, **7**, 740–747.
- 49 S. M. Kim, M. A. Burns and E. F. Hasselbrink, *Anal. Chem.*, 2006, **78**, 4779–4785.
- 50 J. D. Baker, D. T. Kysela, J. Zhou, S. M. Madren, A. S. Wilkens, Y. V. Brun and S. C. Jacobson, *Anal. Chem.*, 2016, **88**, 8476–8483.